The cytoskeleton regulates symmetry transitions in moving amoeboid cells

van Haastert, Peter J M; Keizer-Gunnink, Ineke; Kortholt, Arjan

Published in:
Journal of Cell Science

DOI:
10.1242/jcs.208892

© 2018. Published by The Company of Biologists Ltd | Journal of Cell Science (2018) 131, jcs208892. doi:10.1242/jcs.208892

RESEARCH ARTICLE

The cytoskeleton regulates symmetry transitions in moving amoeboid cells

Peter J. M. van Haastert*, Ineke Keizer-Gunnink and Arjan Kortholt

ABSTRACT

Symmetry and symmetry breaking are essential in biology. Symmetry comes in different forms: rotational symmetry, mirror symmetry and alternating right–left symmetry (for example, gliding reflection symmetry). Especially the transitions between the different symmetry forms are important because they specify crucial points in cell biology, including gastrulation in development, formation of the cleavage furrow in cell division, or the front in cell polarity. However, the mechanisms of these symmetry transitions are not well understood. Here, we have investigated the fundamental properties of symmetry and symmetry transitions of the cytoskeleton during cell movement. Our data show that the dynamic shape changes of amoeboid cells are far from random, but are the consequence of refined symmetries and symmetry changes that are orchestrated by small G-proteins and the cytoskeleton, with local stimulation by F-actin and Scar, and local inhibition by IQGAP2 and myosin.

KEY WORDS: Small G-proteins, Cytoskeleton, Symmetry, *Dictyostelium*, Chemotaxis

INTRODUCTION

The nature of physics is symmetrical. For instance, molecules have equal probability to diffuse to the right or left (Livio, 2012; Gross, 1996). Cells and organisms appear approximately symmetric, unless an input of energy breaks this symmetry to provide specific shapes. The basal cell shape is a sphere that has radial symmetry (can be rotated in any direction around a central point). However, living cells are not perfectly symmetric, because they use energy for metabolism, cell division, shape changes and migration. During cell division, the symmetry gets broken through generation of two poles and a cleavage furrow. During gastrulation, the symmetry of the blastocyst gets broken because of selective movement of some cells. Therefore, symmetry breaking is essential for life (Loh et al., 2016; Goryachev and Leda, 2017; Pillitteri et al., 2016; Rensing, 2016; McDowell et al., 2016; Blum et al., 2014; Wennekamp et al., 2013). Each of these symmetry changes is affected by many signaling components that regulate the cytoskeleton. Here, we have investigated the fundamental properties of shape changes, symmetry and symmetry breaking during cell movement. To identify critical points in shape regulation, we specifically investigated the transition from simple to more complex shapes and the role of different components of the cytoskeleton in these shape changes.

Department of Cell Biochemistry, University of Groningen, Nijenborgh 7, 9747 AG Groningen, The Netherlands.

*Author for correspondence (p.j.m.van.haastert@rug.nl)

P.J.M.v., 0000-0002-8469-0293

Received 24 July 2017; Accepted 19 February 2018

Starvation of *Dictyostelium* cells induces a developmental program that is accompanied by major changes in cell shape. During the first three hours of starvation cells are relatively round, extend protrusions in many directions and are unpolarized. After five hours of starvation, cells become elongated and polarized, because they frequently extend protrusions only at the front of the cell. These polarized cells exhibit a correlated random walk with persistence of cell movement, which facilitates foraging and chemotaxis (Van Haastert and Bosgraaf, 2009; Li et al., 2008; Bosgraaf and Van Haastert, 2009a). We have investigated the molecular mechanism underlying these changes in cell shapes. The actin-based cytoskeleton in the cortex and in protrusions is the major determinant of amoeboid cell shape. The cortex of the cell is a specialized layer of the cytoplasm at the inner phase of the plasma membrane that consists of parallel actin filaments with associated myosin filaments. This acto-myosin network can provide rigidity and facilitates contraction. The cortex of protrusions is depleted in myosin filaments and enriched in Scar–Arp2/3-regulated dendritic actin. The combination of dynamic dendritic F-actin in protrusions and more stable acto-myosin filaments in the cell body provides the mechanism for extensions of the front and contraction of the rear of the cell (Sackmann, 2015; Köster and Mayor, 2016). IQGAP2 is a scaffold protein that is localized at the side of amoeboid cells (Faix and Weber, 2013; Filić et al., 2012). Upon binding to the small GTPase Rac1 it forms a quaternary complex with two cortexillin proteins. The Rac–IQGAP–cortexillin complex interacts with both actin and myosin filaments and thereby regulates the cytoskeleton at the side of the cell (Filić et al., 2014; Sasaki et al., 2007; Lee et al., 2010). This suggests that actin, myosin and IQGAP–cortexillin are the major determinants in regulation of shape changes in amoeboid cells.

Small GTPases play a critical role in regulating the localization and activity of F-actin, myosin and IQGAP, thereby shaping the cell and inducing protrusions. In mammalian cells, the primary players are the aforementioned Rac, and Rho and Cdc42 (Yang et al., 2016; Schwamborn and Püschel, 2004; Goryachev and Leda, 2017). In *Dictyostelium*, the small GTPases Ras and Rac are the major determinants of the regulation of the cytoskeleton (Charest and Firtel, 2006, 2007; Kortholt and van Haastert, 2008; Huang et al., 2013). On the other hand, the cytoskeleton regulates Ras activation (Inoue and Meyer, 2008; Taniguchi et al., 2013; Johnson et al., 2015; Miao et al., 2017; Jin, 2013; Devreotes and Horwitz, 2015; Nichols et al., 2015). By performing a sensitive assay to detect active Ras-GTP in living *Dictyostelium* cells, we have shown that cells in buffer exhibit excitable Ras-GTP patches (van Haastert et al., 2017; Kortholt et al., 2013). In cells treated with Latrunculin A (LatA), which inhibits the F-actin cytoskeleton and makes the cell round and immobile, these patches are relatively small (3 µm), short lived (16 s) and have moderate intensity. Cells in which the F-actin is not inhibited by LatA make protrusions. These cells possess similar excitable small Ras-GTP patches, but these also occur as larger patches; in addition, a new protrusion is always induced at the

Journal of Cell Science (2018) 131, jcs208892. doi:10.1242/jcs.208892

area of the plasma membrane with the strongest Ras-GTP patch (van Haastert et al., 2017; Kortholt et al., 2013). These and other experiments (Miao et al., 2017; Tang et al., 2014; Shi et al., 2013) indicate that Ras–F-actin is a doubly excitable system: Ras itself is excitable, leading to multiple small, short-lived Ras-GTP patches at the boundary of the cell, and Ras–F-actin is excitable leading to one or two large, long-lived and intense Ras-GTP patches in F-actin-filled protrusions (van Haastert et al., 2017). Thus, the shape of the cell, its symmetry and symmetry breaking depend on the underlying spatiotemporal pattern of Ras activation leading to Ras-GTP patches. Here, we have investigated the symmetry of Ras-GTP patches in several cytoskeleton mutants, showing that different components of the cytoskeleton including F-actin, myosin and IQGAP strongly and specifically are involved in transitions between different symmetry forms of Ras activation and changes to the shape of the cell.

RESULTS

Ras patches in three dimensions

To understand excitable Ras activation on the entire surface of the cell, we have investigated Ras activation in three dimensions (3D) (Fig. 1). Sixteen confocal image slices were taken of a *Dictyostelium* cell treated with LatA and that expressed RBD-Raf–GFP and cytosolic RFP, allowing the specific association of RBD-Raf–GFP to Ras–GTP at the membrane (Fig. 1A) to be determined. The cell has a rather round circumference and a slightly compressed height (Fig. 1C). Patches of RBD-Raf–GFP are clearly visible at the boundary of the cell in nearly all slices, whereas the inside of the cell is devoid of RBD-Raf–GFP. These Ras-GTP patches have a normalized intensity of Ψ=0.44±0.17 (mean±s.d., n=20 patches from four cells), whereas the intensity at the boundary in between Ras-GTP patches is Ψ=0.09±0.02 (mean±s.d., n=48 slices from four cells). Slice 2 is of special interest, because it contains the cell–substrate (glass) interface; it contains one RBD-Raf–GFP patch at the boundary (i.e. the cell–glass–liquid interface) and elevated levels of RBD-Raf-GFP at the inside of the boundary in slice 2 (i.e. the cell–glass interface) relative to the inside of all other slices. This suggests that the membrane at the cell–surface interface contains activated Ras-GTP; the normalized fluorescence intensity of this cell–glass interface is Ψ=0.11±0.01 (mean±s.d., n=4 cells), which is very similar to the fluorescence intensity of the boundary outside Ras-GTP patches. In addition to the cell reported in Fig. 1, in 3D analysis of 12 cells we did not observe RBD-Raf–GFP patches at the inner surface of the slice containing the cell–glass interface, only at

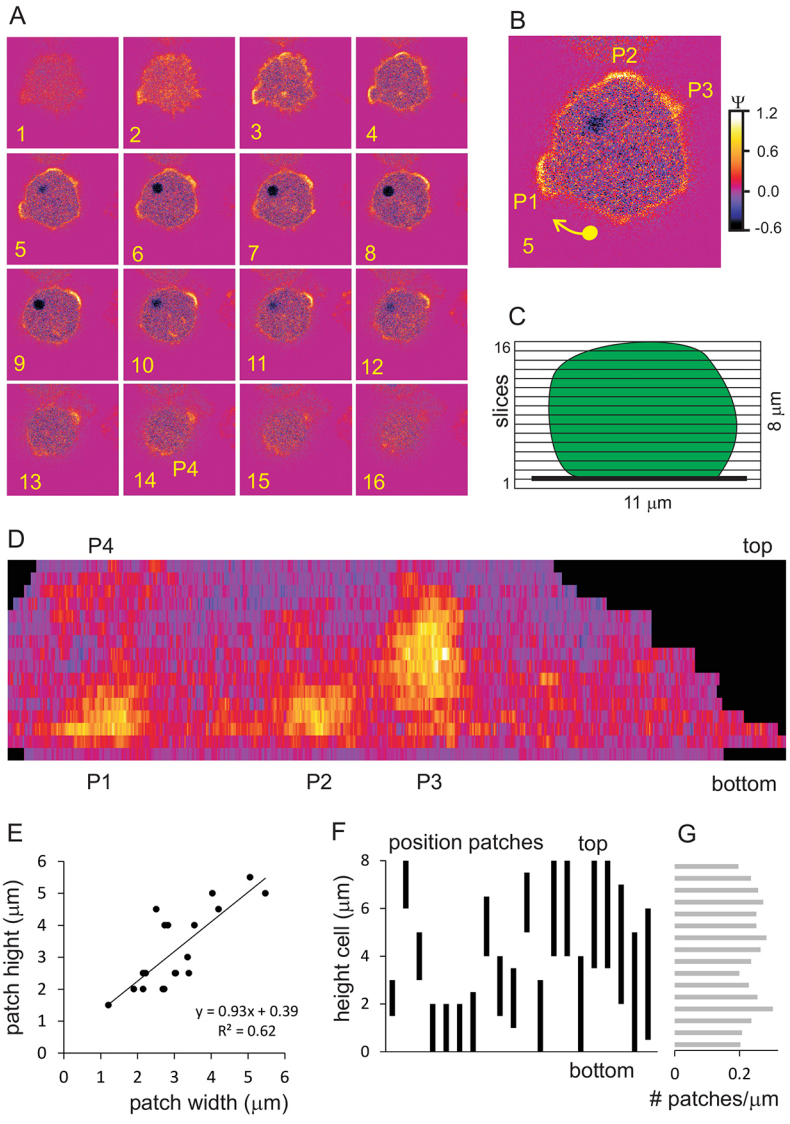

Fig. 1. Three-dimensional activation of Ras in LatA-treated wild-type cells. A series of confocal images in the *Z*-direction were recorded for wild-type cells expressing RBD-Raf–GFP and cytosolic RFP; cells were incubated with 5 µM LatA for 20 min. The RBD-Raf–GFP fluorescence that is associated with the boundary of the cell (Ψ) was calculated for each pixel by subtraction of the RFP signal from the GFP signal (see Materials and Methods). (A) 16 slices of 0.5 µm are presented for a typical cell. (B) Slice 5 (2.0 to 2.5 µm above the glass surface) has indications of three RBD-Raf-GFP patches at the cell boundary; patch P4 is indicated in slice 14 of panel A. (C) Side view of the cell, which is ∼11 µm in maximal diameter and ∼8 µm in height. The glass–cell interface is present in slice 2. (D) Reconstruction of RBD-Raf–GFP at the boundary (Ψ). In each slice, the intensity of RBD-Raf–GFP at the boundary of the cell (Ψ) was determined (clockwise starting south, so that P2 at north is in the middle). The figure shows three major RBD-Raf–GFP patches P1 to P3 and a weaker patch P4. (E) Correlation between width and height of 20 patches from four cells. The correlation is significant at P<0.005. (F) Distribution of patches from bottom to top of the cell. Each black line represents the location of one patch. The patches are ordered arbitrarily from smallest to largest. (G) For each slice, the average number of patches was calculated and divided by the circumference of the cell in that slice, giving the indicated number of patches/µm.

Journal of Cell Science (2018) 131, jcs208892. doi:10.1242/jcs.208892

the edge representing the cell–glass–liquid interphase. We conclude that Ras-GTP patches are present at the cell–liquid interface, but not at the cell–substrate interface. This observation is in agreement with TIRF experiments that specifically probe the cell–surface interface, also showing Ras-GTP patches mainly at the side of the cell at the surface–liquid interface (Charest et al., 2010; Huang et al., 2013).

We recorded the normalized fluorescence at the boundary of all slices and made a two-dimensional (2D) reconstruction of the surface of the spherical cell (Fig. 1D). This cell has four patches (P1–P4); P1 and P2 start at the or just above the bottom and continue to about half-way up the cell, patch P3 is present over nearly the entire height of the cell, whereas patch P4 is present in the upper half of the cell. Data from 20 patches reveal a strong correlation between width and height of patches, indicating that they are approximately round (Fig. 1E). Fig. 1F shows the bottom–top localization of these 20 patches revealing no specific preference. The four cells analyzed in 3D contain on average 2.0±0.3 patches/slice and 4.8±0.5 patches/cell; patches have a width of 3.1±1.1 µm, a height of 3.2±1.3 µm and a mean intensity of Ψ=0.44±0.17. This is consistent with our previous analysis of Ras-GTP patches in confocal slices showing 2.2±0.8 patches/slice, with a width of 2.9±1.2 µm, and a mean intensity of Ψ=0.33±0.14 (van Haastert et al., 2017). We conclude that a cell treated with LatA contains approximately round excitable Ras-GTP patches at its cell–liquid interface. The total surface area of Ras-GTP patches of a cell is on average 37 µm^2, which is ∼10% of surface area of the liquid–cell interface.

Activation of Ras, Rap and Rac and presence of F-actin

We have quantified the activation of Ras, Rap, Rac and F-actin because these proteins have been shown to regulate each other in a complex network and because they are located at similar places in the cell. We used the sensors RBD-Raf–GFP for Ras-GTP, Ral-GDS–GFP for Rap1-GTP, CRIB–GFP for Rac-GTP and LimE–RFP for F-actin. Unfortunately, visualizing direct colocalization of Ras, Rap and Rac with F-actin is difficult because RFP versions of these sensors are not expressed well in *Dictyostelium*. Therefore, we co-expressed the GFP sensors for Ras and Rap with cytosolic-localized RFP to obtain highly sensitive images for the relatively modest activation of Ras and Rap, and we co-expressed CRIP–GFP and LimE–RFP to determine the colocalization of the more pronounced activation of Rac-GTP with F-actin. Unpolarized cells (Fig. 2A–F) possess an equal number or Ras, Rap1 and Rac patches (about three patches, Fig. 2D); these patches are present predominantly in concave extensions of the cell (Fig. 2A–C). The width of the Rap and Rac patches are larger than in Ras patches (Fig. 2E). The intensity of Rap patches (Ψ=0.60±0.19) and especially the intensity in between the patches (Ψ=0.33±0.11) is higher for Rap-GTP compared to Ras-GTP (Ψ=0.40±0.11 for patches and Ψ=0.16±0.16 in between patches). Rac activation of Ψ=1.6±0.6 in patches is much stronger than the activation of Ras and Rap. Fig. 2C presents the colocalization of activated Rac-GTP with F-actin measured with the sensors CRIB–GFP and LimE–RFP, respectively. From the analysis of 26 cells, we observed 83 Rac-GTP patches and 101 F-actin patches. Furthermore, we observed that 81 out of 83 of the Rac-GTP patches are tightly associated with an F-actin patch; interestingly, these F-actin patches (2.7±1.0 µm) are significantly smaller than the associated Rac patches (6.2±3.3 µm). Since cells contain more F-actin than Rac-GTP patches, 20 out of 101 F-actin patches are not associated with a patch of Rac-GTP.

Polarized cells have one strong Ras-GTP patch at the leading edge and often multiple far smaller patches at the side of the cell (Fig. 2G,J). Rap-GTP is also localized in the front of the cell, but over a much larger area: half-maximal Ras activation is restricted to the front of the cell (26° to the left and right of the front, which represents 15% of the circumference of the cell), while half-maximal Rap activation extends to the front 50% of the circumference (Fig. 2H,J). Interestingly, Rac activation and F-actin are present in the same small region of the front of the cell as Ras. Besides a strong patch at the front, F-actin is also present in small patches in the rear of the cell and at the side of the cell (Fig. 2I,K).

In summary, the places showing Ras activation are nearly always associated with the activation of Rap and Rac and F-actin. F-actin is also present outside regions of Rac activation (in the rear and at the side of the cell), and Rap shows a relatively high level of basal activation in the entire membrane and is activated in a very large patch at the front of a polarized cell.

Ras activation in cytoskeletal mutants

In early unpolarized cells, RBD-Raf–GFP is localized in small areas at the cell boundary representing patches of activated Ras-GTP (Fig. 3A). These Ras-GTP patches are of similar size and are approximately equally spaced from each other. In contrast, late starved cells have one strong RBD-Raf–GFP patch at the leading edge and a few smaller patches at the side of the cell (Fig. 3B). Addition of the F-actin inhibitor LatA does not eliminate RBD-Raf–GFP patches, but reduces their intensity (images and line scans in Fig. 3A), consistent with previous observations showing that F-actin stimulates Ras-GTP activation (van Haastert et al., 2017; Sasaki et al., 2007; Huang et al., 2013; Miao et al., 2017).

Cells with a deletion of the gene encoding myosin II (*myoII*-null, see Materials and Methods for precise details of genes that have been deleted) lack the myosin-based contraction in the rear of the cell (Bosgraaf and van Haastert, 2006; Meili et al., 2010); such cells remain unpolarized, even after prolonged starvation. In these cells, RBD-Raf–GFP is localized in multiple patches as in early wild-type cells (Fig. 3C). Cells with a deletion of the gene encoding IQGAP2 exhibit a very different phenotype, showing very high and nearly uniform localization of RBD-Raf–GFP at the boundary of the cell (Fig. 3D). These *iqgap2*-null cells have strongly elevated levels F-actin in multiple projections (Lee et al., 2010), consistent with a positive-feedback loop between F-actin polymerization and Ras activation. Addition of LatA to *myoII*-null or *iqgap2*-null cells inhibits Ras activation, as in wild-type cells, but the effects are much stronger (Fig. 3E). In wild-type cells LatA treatment reduces the intensity of the Ras-GTP patches, but not their number per cell (van Haastert et al., 2017). However, in *myoII*-null and *iqgap2*-null cells the number of patches is strongly reduced from 2.2 patches/cell in wild-type to 0.78 and 0.39 patches/cell in *iqgap2*-null and *myoII*-null cells, respectively (Fig. 3E). Interestingly, in these LatA-treated cells the intensity and width of the rare Ras-GTP patches in *myoII*-null and *iqgap2*-null cells is not different from that seen in wild-type cells (Fig. 3E), suggesting that these mutants exhibit a strongly reduced propensity to form Ras-GTP patches, but once patches are induced, their intensity is not different from the many Ras-GTP patches of wild-type cells.

Rotation and reflection symmetry

We next quantified the magnitude of the RBD-Raf–GFP patches in wild-type and mutant cells, as well as the heterogeneity in patches and the type of symmetry (Fig. 4; see also Table S1, and the Materials and Methods for definitions of radial, rotational, reflection and gliding symmetry). The mean level of Ras-GTP at the boundary is given as the parameter <Ψ>. All cell lines have a similar mean activation of Ras (<Ψ>=∼0.3), and in all cases LatA leads to a

Journal of Cell Science (2018) 131, jcs208892. doi:10.1242/jcs.208892

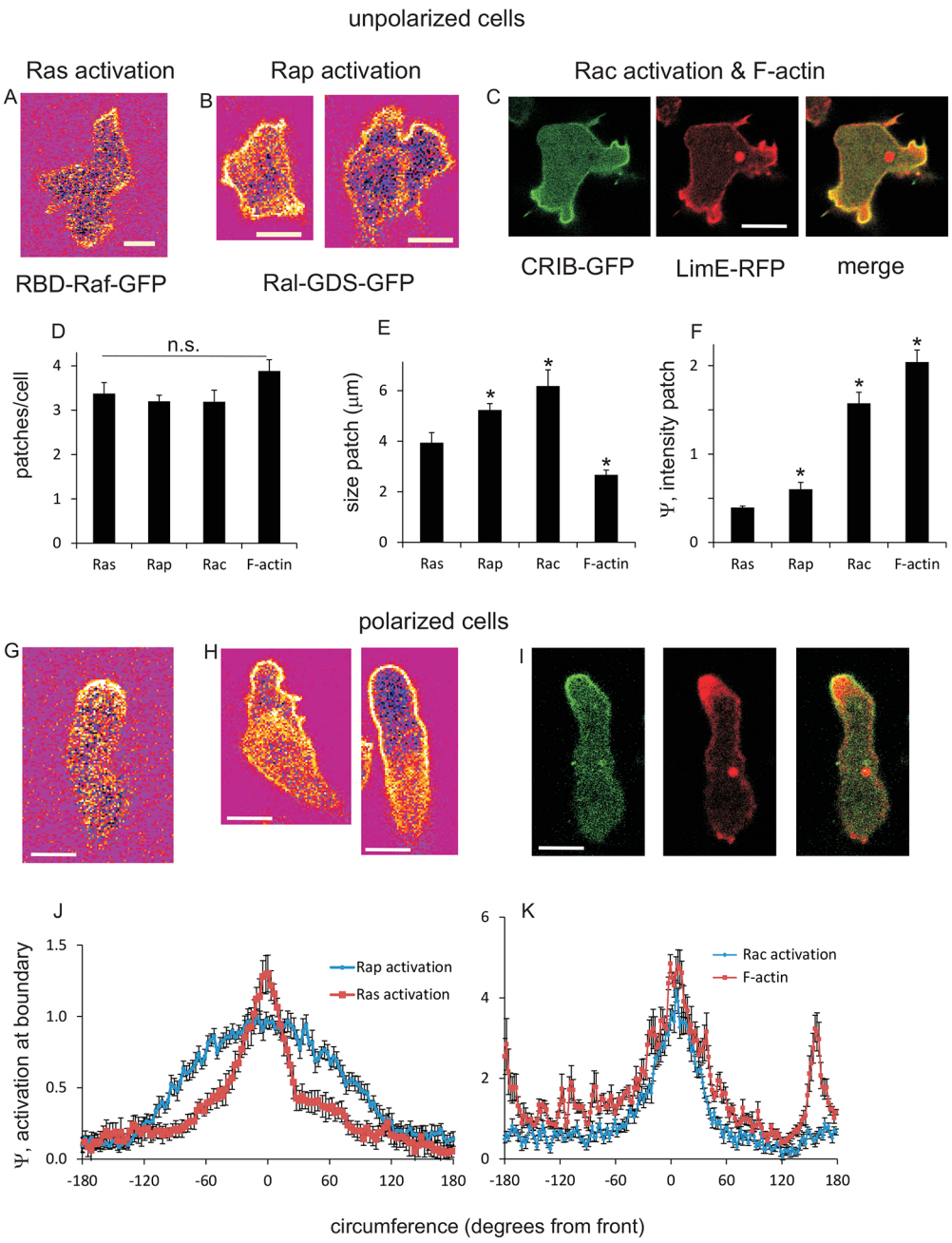

Fig. 2. Localization of activated Ras, Rac, Rap and F-actin in unpolarized and polarized cells. Wild-type cells expressing RBD-Raf–GFP and cytosolic RFP for determination of Ras activation (A and G), Ral-GDS–GFP and cytosolic RFP for determination of Rap activation (B and H), or expressing CRIB–GFP and LimE–RFP for determination of Rac activation and the presence of F-actin, respectively (C and I). Unpolarized and polarized cells were starved for 3 and 6 h, respectively. A, B, G and H show fluorescence that is associated with the boundary of the cell (Ψ), which was calculated for each pixel by subtraction of the RFP signal from the GFP signal (see Materials and Methods). Note that the cell in A is reproduced from fig. 1A in van Haastert et al. (2017). It is also used for analysis in Fig. 3A, Fig. S3A and Fig. 7A. C and I show colocalization of Rac-GTP and F-actin. (D–F) Mean±s.e.m. values for the number of patches per cell, and the size and intensity of patches as measured for 53, 30, 27 and 30 patches and 16, 35, 24 and 24 cells for Ras, Rap, Rac and F-actin, respectively (*P<0.01 compared with from Ras). (J,K) The intensity at the boundary (mean±s.e.m. for 10 cells). Scale bars: 5 μm.

similar reduction of Ras activation (<Ψ>=∼0.1; Fig. 4A). The parameter ζ indicates the heterogeneity of Ras-GTP activation; ζ is defined as the relative variance of Ψ. The data (Fig. 4B) clearly show that all cell lines have very large heterogeneity that is characterized by Ras-GTP patches, except for *iqgap2*-null, *iqgap2*-null+LatA and *myoII*-null+LatA cells, which have near-uniform localization of activated Ras-GTP. The *iqgap2*-null cells have many F-actin and Ras-GTP filled protrusions that are responsible for the rather uniform but high level of Ras activation. In the presence of LatA most *myoII*-null and *iqgap2*-null cells do not exhibit Ras-GTP patches and therefore they exhibit a rather uniform but low level of Ras activation.

For the cell lines that possess Ras-GTP patches, we mathematically and statistically determined the type of symmetry (see Materials and Methods, see Fig. 7 and Figs S2–S4). Fig. 4C indicates the probability that the spatial distribution of the Ras-GTP patches is best explained by rotational symmetry or by reflection symmetry. The results reveal that early starved wild-type cells and *myoII*-null cells have rotational symmetry, whereas late starved wild-type cells have reflection symmetry. These symmetries in wild-type cells are not affected by LatA. Thus, although LatA inhibits the magnitude of Ras activation, the activation still occurs in patches, retaining the type of symmetry. The symmetry of wild-type cells is further analyzed in Fig. S1, demonstrating that starved cells are truly polarized cells, because reflection symmetry is characterized by an odd number of patches (one at the leading edge, none in the rear, and an equal number of patches at either side of the cell), and the intensity of the patches declines as the distance from the leading edge of the cell increases. In contrast, in early starved cells, all patches have similar intensities and the number can be odd or even, characterizing the early cells as unpolarized.

Journal of Cell Science (2018) 131, jcs208892. doi:10.1242/jcs.208892

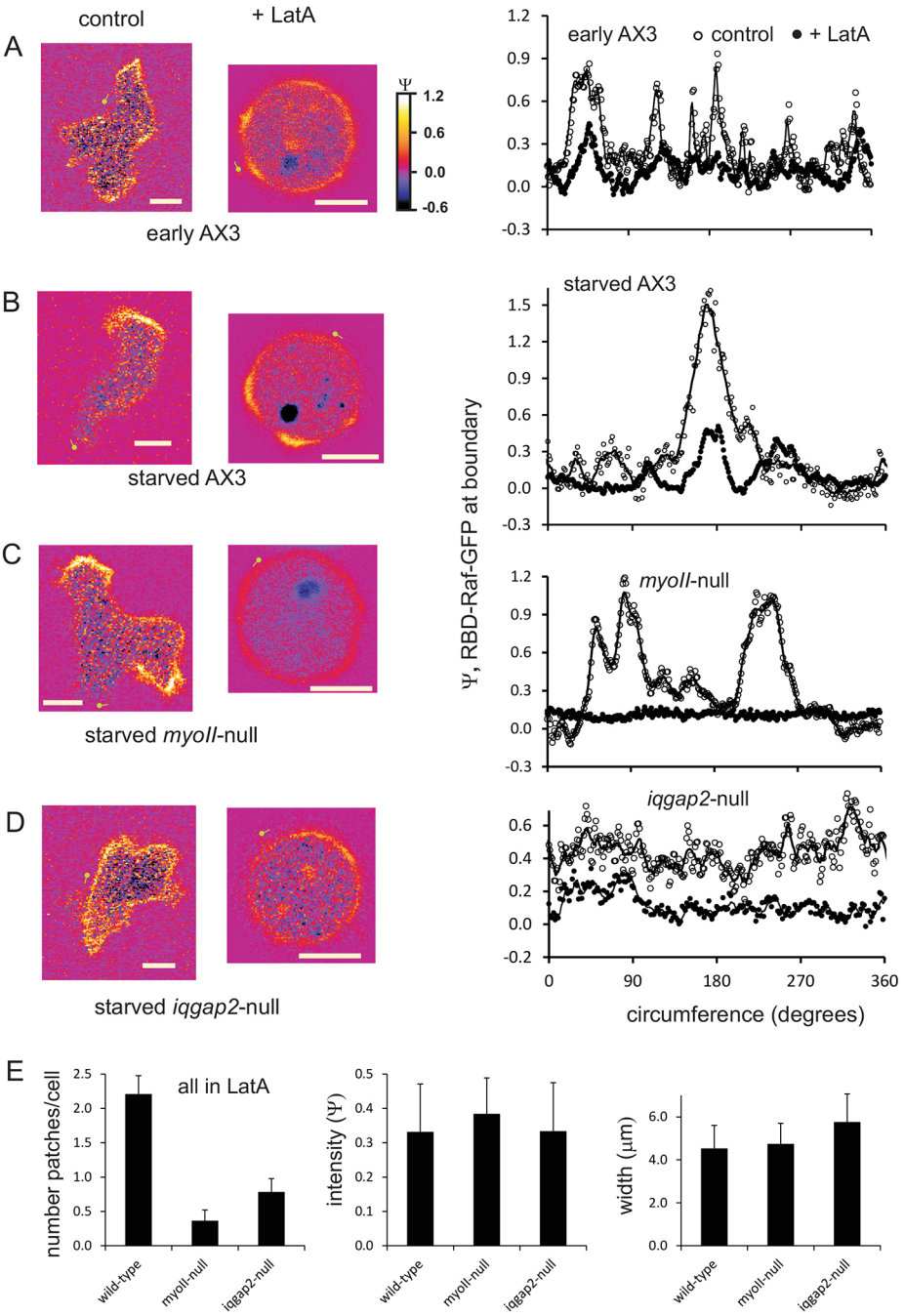

Fig. 3. Ras activation in actin-associated cytoskeleton mutants. Movies of cells expressing RBD-Raf–GFP and cytosolic RFP were recorded by means of confocal fluorescence microscopy. The RBD-Raf–GFP fluorescence that is associated with the boundary of the cell (Ψ) was calculated for each pixel by subtraction of the RFP signal from the GFP signal (see Materials and Methods). Left panels show representative images of wild-type or mutant cells under the conditions indicated. All images are presented at the indicated color scale from −0.6 to 1.2. Scale bars: 5 µm. Right panels show Ψ at the boundary of these cells, starting from the green dot in the cell images. Open and closed circles are without and with LatA, respectively. (A) Unpolarized wild-type cells starved for 3 h. Note that the same cell is also used for analysis in Fig. 2A, Fig. S3A and Fig. 7A. (B) Polarized wild-type cell starved for 6 h. (C) Mutant *myoII*-null starved for 6 h; the cell in LatA has no Ras-GTP patch. (D) Mutant *iqgap2*-null cell starved for 6 h; the cell in LatA has one Ras-GTP patch. (E) Analysis of the Ras-GTP patches of wild-type and mutant cells in the presence of LatA. Mutant cells in LatA have significantly fewer patches than wild-type cells ($P<0.05$). The intensity and width are not significantly different (all at $P>0.05$). The number of patches per cell was recorded in sections of 21 frames; data are mean±s.d. of 10 sections. The width and intensity was measured in cells with one patch (to be comparable between wild-type and mutants that usually have only one patch); data are from 28, 11 and 18 patches from wild-type, *myoII*-null and *iqgap2*-null cells all in LatA, respectively.

Left–right asymmetry

Closer inspection of cell movement in polarized cells revealed a left–right bias (Bosgraaf and Van Haastert, 2009b; Li et al., 2008). Cells preferentially extend new pseudopods alternatingly to the right and left (Fig. 5A). This left–right bias induces a gait with persistence of direction (Bosgraaf and Van Haastert, 2009b; Li et al., 2008). Fig. 5B shows the localization of Ras-GTP in cells that all are in the process of extending a pseudopod to the left. In addition to the strong patch of activated Ras in the extending pseudopod, a smaller patch of activated Ras is present at the right side of this pseudopod, where the previous pseudopod was extended and the next pseudopod is expected to be formed. Importantly, one pseudopod later, the smaller Ras-GTP patch at the right is converted into the strongest patch with the new pseudopod, while the old strong patch has declined to being a small patch that is now present at the left side of the strongest Ras patch. The experiment thus reveals that the reflection symmetry is broken transversally at a specific moment in time. This type of symmetry is called gliding reflection symmetry, as in human gait where the right and left foot obtain reflection symmetry after gliding back the forward footstep to an opposing position.

We have quantified the left–right asymmetry of Ras-GTP patches by measuring the difference of intensity of the two Ras-GTP patches at the left and right side of the strongest Ras-GTP patch (see Materials and Methods for details). Fig. 4D reveals that these opposing patches are different from each other by ∼25% for both early and late wild-type cells. In contrast, the opposing Ras-GTP patches are nearly identical in LatA. This is in agreement with previous suggestions that F-actin, or one of its binding proteins, mediates right–left asymmetry (van Haastert et al., 2017). We

Journal of Cell Science (2018) 131, jcs208892. doi:10.1242/jcs.208892

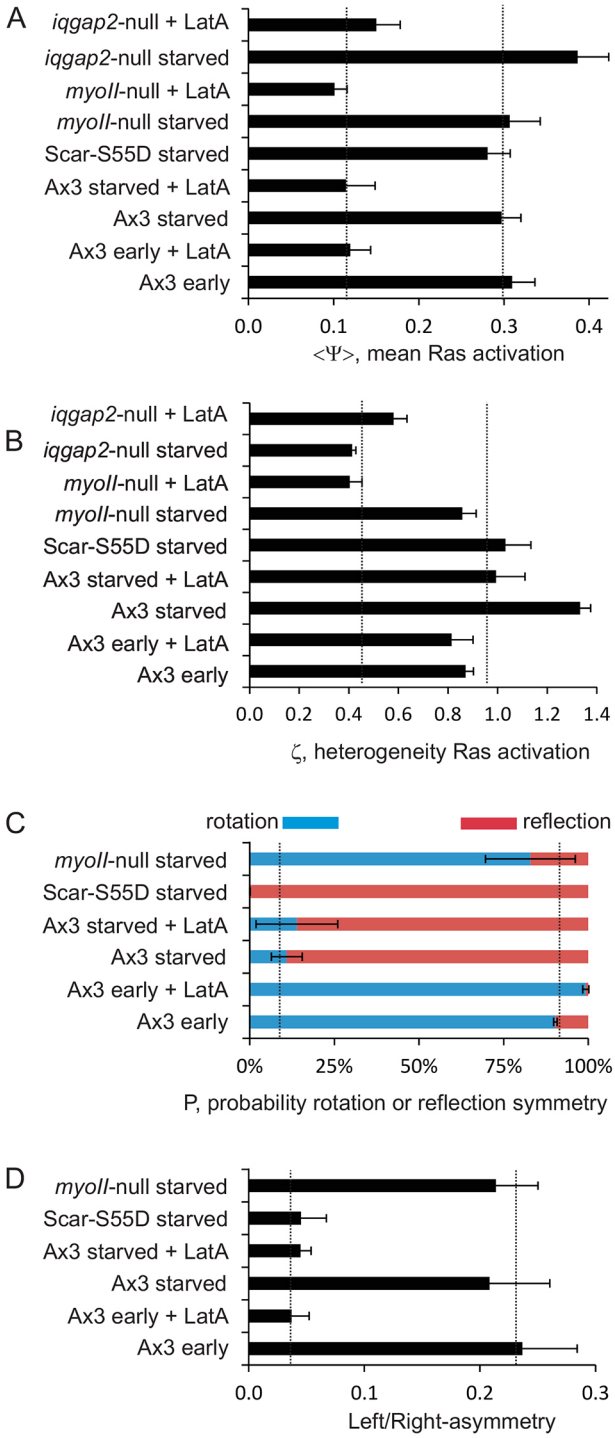

Fig. 4. Symmetry of Ras activation in actin-associated cytoskeleton mutants. The level of Ras activation along the boundary of the cell (Ψ) was determined for at least eight cells as indicated in the line drawings of Fig. 1. (A,B) For each cell we determined the mean (named <Ψ>) and relative standard deviation (named ζ) of Ψ. (A) The mean±s.d. of <Ψ>, as a measure of the mean Ras activation. The dotted lines show that cells in LatA have low Ras activation, while all cells without LatA have strong Ras activation. (B) The mean±s.d. of the relative standard deviation ζ of Ψ as a measure of the heterogeneity of Ras activation. The dotted lines show that Ras activation in *iqgap2*-null cells (with or without LatA) and *myoII*-null+LatA cells has low heterogeneity (is uniform), while all other cells have strong heterogeneity. (C) The probability that the observed heterogeneity is associated with rotational or reflection symmetry (see Materials and Methods for details). The dotted lines show that early AX3 and starved *myoII*-null cells have rotational symmetry, while starved AX3 and Scar-S55D cells have reflection symmetry. (D) The asymmetry between right and left. The difference of intensity of the two Ras-GTP patches at the left and right side of the strongest Ras-GTP patch relative to the sum of the intensities of these two patches (see Materials and Methods) was measured. The dotted lines show that cells in LatA and Scar-S55D are left–right symmetric, while the other cell lines are asymmetric.

investigated left–right asymmetry in many signaling and cytoskeletal mutants (Fig. 5C). *rasC*-null cells expressing the dominant-negative mutant RasG-S17N have a very low activation of RasG and RasC (Kortholt et al., 2013), but show normal alternating left–right bias. In addition, all of the cytoskeletal mutants tested (deletions of arpin, mDia, cortexillin A and B, IQGAP1, IQGAP2, myosin II and dynacortin) have normal alternating left–right bias (Fig. 5C). However, Scar appears to be involved in right–left asymmetry. The *scar*-null cells rather exhibit normal alternating left–right bias, which may be related to the complex compensation of the missing Scar protein by Wave and formins (Davidson et al., 2017). Surprisingly *scar*-null cells expressing the phosphomimic Scar-S55D extends pseudopods that have no preference for alternating right–left (Figs 4D and 5C). In conjunction, the Ras-GTP patches in these Scar-S55D cells have no left–right asymmetry (Fig. 5B). This suggests that Scar introduces the third symmetry breaking. It stimulates F-actin and Ras activation at the position of the previously extinguished pseudopod by which a transversal axis appears and reflection symmetry converts to gliding reflection symmetry.

DISCUSSION

The shape of amoeboid cells is very dynamic and depends primarily on the actin-based cytoskeleton. A simple shape is an unpolarized cell with protrusions in all directions, characterized by rotational symmetry. A more complex shape is a polarized cell with a relatively inactive rear and protrusions extended from the front of the cell; such cells have lost rotational symmetry and often obtain reflection symmetry. A still more complex shape may arise when cells move; in *Dictyostelium* cells the protrusions are formed at the front alternatingly to the right and left, representing the more complicated gliding reflection symmetry. Each of these symmetry forms is affected by many signaling molecules, which makes it difficult to understand how signaling to the cytoskeleton shapes the cell dynamically. By studying the cytoskeletal requirements for the transition from simple to more complex forms, and not for the symmetry forms per se, we aimed to identify the critical component(s) in symmetry and symmetry breaking.

A model for phase separation and symmetry breaking of the actin-based cytoskeleton

Fig. 6 summarizes the observations on symmetries and symmetry breakings. In the signaling schematic of Fig. 6A, these observations are combined with published biochemical characterizations of myosin II and IQGAP2–cortexillin (Jeon et al., 2007; Bosgraaf and van Haastert, 2006; Lee et al., 2010; Filić et al., 2012, 2014; Kee et al., 2012). It has been well documented that activated Ras-GTP induces dendritic F-actin filament formation, most likely via activation of Rac, Scar and the Arp2/3 complex (Krause and Gautreau, 2014; Insall, 2013; Köster and Mayor, 2016). Ras activation is excitable, leading to small short-lived Ras-GTP patches in cells treated with LatA (van Haastert et al., 2017 and Fig. 3). Here, we showed that in the absence of the F-actin cytoskeleton (*myoII*-null+LatA or *iqgap2*-null+LatA) excitability is very low, and although Ras-GTP patches are rare, when they are

Journal of Cell Science (2018) 131, jcs208892. doi:10.1242/jcs.208892

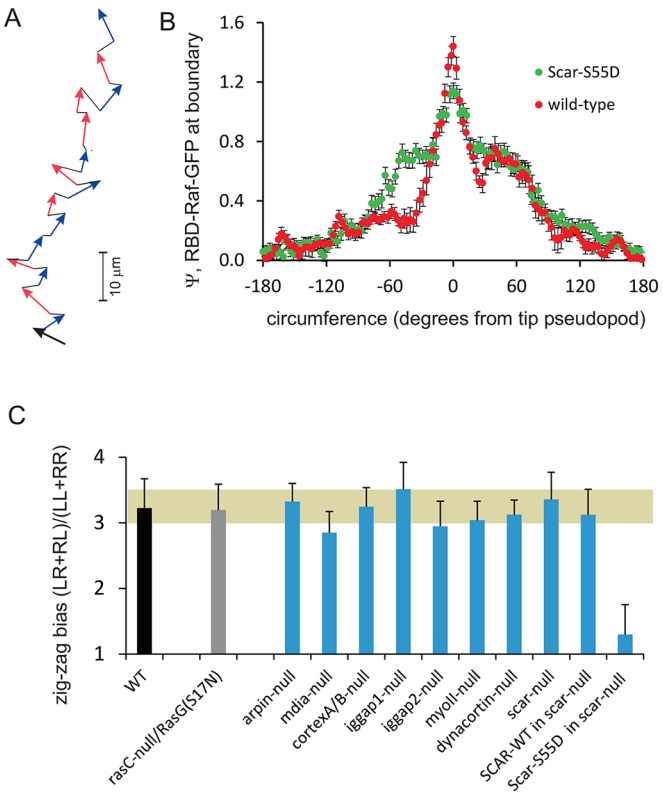

Fig. 5. Left–right asymmetry in wild-type and mutant cells. (A) Track of representative starved wild-type cells. The arrows show the pseudopods. Blue arrows indicate pseudopods that start at the right side relative to where the previous pseudopod has stopped, red arrows start at the left side. The track reveals a zig-zag pattern with many alternating left–right extensions of pseudopods. (B) Left–right asymmetry of Ras activation. RDB-Raf–GFP at the boundary was determined in cells that all are in the process of extending a pseudopod to the left. The tip of the pseudopod is at 0 degrees. The figure shows that both cell lines have the strongest patch of activated Ras in the extending pseudopod; wild-type cells also exhibit a stronger patch at the right side (where the previous and next pseudopod is expected to be extended) than at the left side. Scar-S55D in *scar*-null cells are left–right symmetric. Data are the mean±s.e.m. of 19 images from eight different cells (wild-type) or 27 images of nine different cells (mutant) with *n*=the number of images. Note that the wild-type data are reproduced from fig. 5B in van Haastert et al. (2017). (C) Left–right asymmetry of pseudopod extensions of different cell lines determined in during long tracks of movement (>10 pseudopods); data are the mean±s.d. of 12 tracks. The gray bar represents the mean±s.d. of all cell lines except those expressing Scar-S55D in *scar*-null cells. The figure shows that cells expressing Scar-S55D in *scar*-null cells exhibit left–right bias that is statistically not significantly different from 1.0 (random).

present they have the characteristic small short-lived properties (Fig. 3E). Thus, in the absence of the cytoskeleton, cells have low uniform Ras-GTP levels and occasionally Ras-GTP patches (Fig. 6B). Interestingly, *iqgap2*-null cells in buffer (no LatA) do not exhibit Ras-GTP patches; instead strong Ras activation occurs at the entire boundary of the cell (Fig. 3D). This suggests that the positive-feedback loop between Ras, Rac and F-actin (arrows labeled 1 in Fig. 6A) leads to rather uniform activation of F-actin (Lee et al., 2010) and Ras in *iqgap2*-null cells (Fig. 6C). It has been demonstrated that F-actin inhibits IQGAP–cortexillin complex (arrow 2) (Mondal et al., 2010; Filić et al., 2012), and that IQGAP binds and thereby sequesters Rac (arrow 3) (Filić et al., 2014). The combination of 1–3 implies phase separation of F-actin and IQGAP2: at places where IQGAP2 is localized, Rac sequestration inhibits F-actin formation, whereas at places where there is a large amount of F-actin, IQGAP2 is inhibited, which allows F-actin to exist. Ras activation by F-actin and inhibition by IQGAP2 induces rotational symmetry (Fig. 6D). The inhibition by IQGAP2 probably keeps the patches separated from each other. We have analyzed in the few *iqgap2*-null+LatA cells that have multiple Ras-GTP patches how well these patches are separated by determining the symmetry factor *s* (see Materials and Methods, *s* is between 0 and 1; *s*=0 for perfect symmetry). We observed *s*=0.16±0.04, *n*=12 for *iqgap2*-null+LatA cells, which is significantly higher (less symmetric) that wild-type cells that have *s*=0.08±0.03, *n*=14 ($P<0.01$). Furthermore, we observed that Ras-GTP patches in LatA are 'wiggling', but generally stay separated in wild-type+LatA cells, in contrast to what is seen in *iqgap2*-null+LatA cells, where they frequently merge during the 30 min incubation with LatA.

The rotational symmetry that is induced by F-actin and IQGAP2 changes to reflection symmetry by myosin II (Fig. 6E). In polarized *Dictyostelium* cells, myosin filament formation is regulated by cGMP through the cGMP-binding protein GbpC (arrows labeled 4 in Fig. 6A) (Bosgraaf and van Haastert, 2006); in mammalian cells, myosin is regulated similarly by the Rho kinases (Kureishi et al., 1997; Kimura et al., 1996). The rapidly diffusible cGMP induces myosin filament formation in the entire cell. In addition, myosin filaments are formed at the side of the cell through the action of the IQGAP2–cortexillin complex (arrow 5 in Fig. 6A) (Ren et al., 2009). Rap-GTP is activated by Ras-GTP and induces the disassembly of myosin filaments, which occurs in the front of the cell (arrow 6) (Jeon et al., 2007; Kortholt and van Haastert, 2008). Myosin filaments inhibit the formation of dendritic actin filaments (arrow 7) (Ngo et al., 2016). The combination of processes 4–7 implies that myosin filaments are only present in the rear and at the side of the cell, and that formation of dendritic actin filaments are inhibited in the back but not in the front of the cell. The stable formation of myosin filaments in the rear induces a longitudinal front–rear axis of Ras activation leading to a polarized cell with reflection symmetry (Fig. 6E).

In this model, IQGAP2–cortexillin at the side of the cell plays a critical role in phase separation between the front and rear of the cell. Rac1 has an intriguing role in phase separation. Binding of Rac1 to IQGAP2 induces the formation of a quaternary complex with two cortexillin molecules that induce formation of myosin filaments (Ren et al., 2009). The IQGAP2–Rac1 complex has a very long lifetime, during which time these Rac1 molecules are not available for activating F-actin (Filić et al., 2014). Thus, the IQGAP2–cortexillin–Rac1 complex at the side of the cell is simultaneously a Rac1 effector for myosin filament formation and a Rac1 inhibitor through sequestration for F-actin formation. In this way, the IQGAP2–cortexillin separates the F-actin-rich front from the myosin-rich rear.

Finally, the reflection symmetry is transversally broken in time leading to the alternating left–right extension of a protrusion, leading to gliding reflection symmetry (Fig. 6F). A protrusion is extended at a similar position of the cell surface as a 'pre-previous protrusion', suggesting that this pre-previous protrusion has left behind a memory of protrusion-inducing activity. Experiments with mutant Scar-S55D and the biochemistry of Scar activation (Ura et al., 2012; Davidson and Insall, 2013) suggest that the dynamics of Scar phosphorylation and dephosphorylation may provide a mechanism for this memory and the accompanying transient transversal symmetry changes.

In summary, by investigating the mechanisms by which cells with simple symmetry forms convert into having more complex symmetry forms, we have identified critical roles of F-actin,

Journal of Cell Science (2018) 131, jcs208892. doi:10.1242/jcs.208892

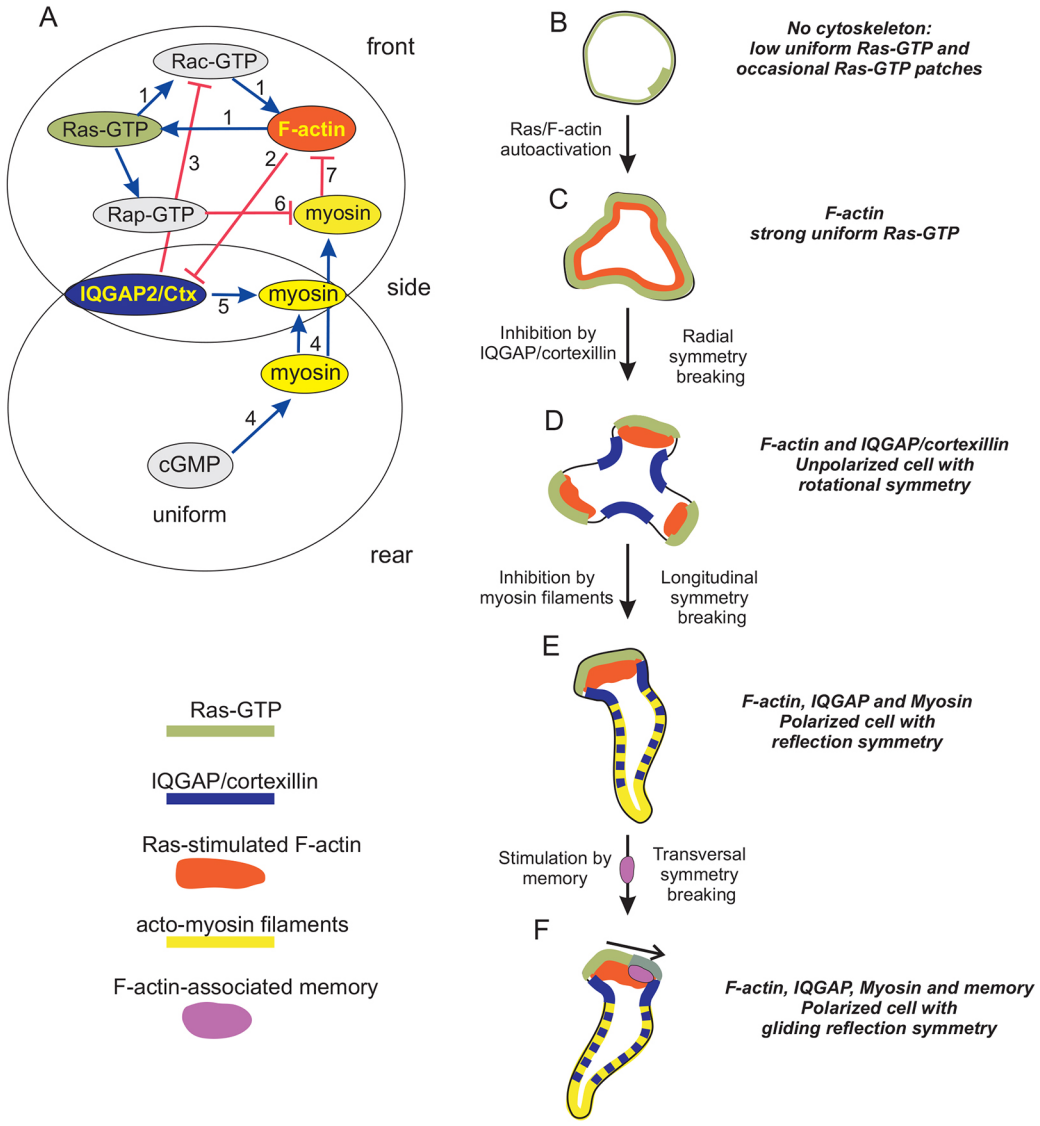

Fig. 6. Model and functions of symmetry and symmetry breaking. (A) Schematic. The numbers refer to the following steps. (1) The positive-feedback loop between Ras, Rac and F-actin leading to rather uniform activation of F-actin. (2) F-actin inhibits the IQGAP2–cortexillin (IQGAP2/Ctx) complex. (3) IQGAP2 binds and thereby sequesters Rac. (4) The rapidly diffusible cGMP induces myosin filament formation in the entire cell. (5) The Rac–IQGAP2–cortexillin complex at the side of the cell induces myosin filament formation. (6) Rap-GTP is activated by Ras-GTP and induces the disassembly of myosin filaments, which occurs in the front of the cell. (7) Myosin filaments inhibit the formation of dendritic actin filaments. (B–F) Symmetry breaking. (B) In the absence of the F-actin-based cytoskeleton (i.e. *myoII*-null+LatA), Ras activation is either low and uniform, or comprises a few small short-lived Ras-GTP patches. (C) Activation of Ras and formation of F-actin filaments form a mutual positive-feedback loop. In the absence of IQGAP2 and myosin II, this leads to uniform Ras and F-actin activation. (D) The IQGAP2–cortexillin complex at the side of the cell inhibits Ras activation, which induces symmetry breaking of uniform Ras-GTP thereby leading to patches of activated Ras with rotational symmetry in unpolarized cells. (E) Myosin filaments in the rear of the cell inhibit F-actin and/or Ras activation, which induces symmetry breaking of rotational symmetry, thereby inducing a polarized cell with a longitudinal axis and reflection symmetry. (F) Left–right asymmetry is induced by a component of the F-actin-regulating machinery of the extending protrusion, presumably the phosphorylation state of Scar. This transversal symmetry breaking leads to the gliding reflection symmetry that is typical for the alternating right–left gait of polarized cells.

IQGAP2, myosin and Scar in the transition from rotational to gliding reflection symmetry. This series of symmetry breakings by the actin-based cytoskeleton induces the polarized cell in which pseudopod extensions are restricted to the front of the cell, while 'memory' induces these pseudopods to be extended alternatingly to the left and right. Together, they are responsible for the persistence of cell movement and the correlated random walk. In conclusion, it appears that the dynamic shape changes of amoeboid cells are far from random, but are the consequence of refined symmetries, symmetry changes and memory that is orchestrated by Ras, Rac, Rap, IQGAP2, Scar, myosin and F-actin.

MATERIALS AND METHODS

Cell lines and preparation

The cell lines used are the wild-type AX3 and the mutants *myoII*-null with a deletion of the *mhcA* (DDB_G0286355) gene (Ruppel et al., 1994), *iqgap1*-null with a deletion of the *iqgA* (DDB_G0287585) gene and *iqgap2*-null with a deletion of the *iqgB* (DDB_G0269140) gene (Lee et al., 2010), *mDia*-null with a deletion of the *forA* (DDB_G0279607) gene (Ramalingam et al., 2015), *dynacortin*-null with a deletion of the *dct* (DDB_G0283767) gene (Girard et al., 2004), cortexillin A/B-null with a deletion of the ctxA (DDB_G0289483) and ctxB (DDB_G0276893) gene (Lee et al., 2010), *scar*-null cells with a deletion of the *scrA* (DDB_G0285253) gene (Ura et al., 2012), *arpin*-null cells with a deletion of the *arpin* (DDB_G0291009)

Journal of Cell Science (2018) 131, jcs208892. doi:10.1242/jcs.208892

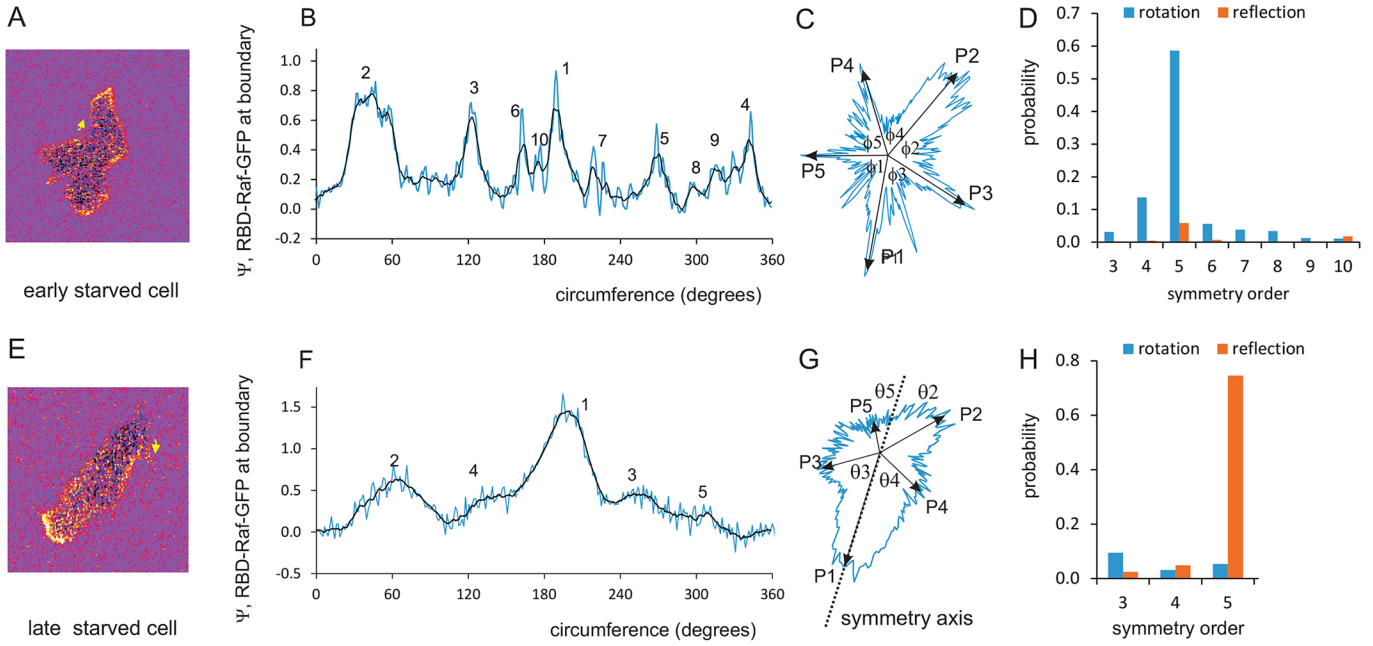

Fig. 7. Calculation and example of rotational symmetry and reflection symmetry. (A,E) RBD-Raf–GFP without cytosolic RFP in unpolarized (A) early starved 3 h cells and polarized (E) late starved 5 h cells. Note that the cell in A is reproduced from fig. 1A in van Haastert et al. (2017). It is also used for analysis in Fig. 2A, Fig. 3A and Fig. S3A. Cell in E is also analyzed in Fig. S4A. (B,F) RBD-Raf–GFP levels at the boundary of the cell (Ψ), starting at the yellow arrow in the cell image. The ten largest patches (B) or five largest patches (E) are numbered sequentially with decreasing intensity. (C,G) The five largest patches are indicated with intensity P_i. In C, all five patches are treated identically (rotational symmetry) with angle ϕ_i to the next patch (arbitrarily to the right). In F, a line of reflection symmetry is drawn through the largest patch P1, and patches are treated as pairs with angle θ_i to the line of symmetry. (D,H) The Akaike Information Criterion (AIC) was used to calculate the probability that the data are explained by rotation or reflection symmetry with the indicated order. The distribution of Ras-GTP patches is best explained by rotational symmetry of order five for the early starved unpolarized cell and by reflection symmetry with order five for the late starved polar cell. See Materials and Methods, and Figs S3 and S4 for details.

gene (Dang et al., 2013), Scar-S55D in *scar*-null cells (Ura et al., 2012) and RasG-S17N in *rasC*-null cells (Kortholt et al., 2013). To study Ras activation, RBD-Raf–GFP was co-expressed with cytosolic mRFP in wild-type AX3 or mutant cells from a single plasmid (Kortholt et al., 2013). To monitor Rap1 activation, cells were transformed with a modified version of plasmid pDK323Ral-GDS-GFP (Plak et al., 2014), in which cytosolic RFP was introduced in the NgoMIV site. For determining the colocalization of Rac activation and F-actin, cells expressing PakB-CRIB–GFP and LimEΔcoil–RFP (Veltman et al., 2016). Cells were grown in HL5-C medium including glucose (ForMedium), containing the appropriate antibiotics for selection of the parental strains and 50 µg/ml Hygromycin B (Invitrogen) for selection of the GFP or mRFP expression plasmids. Cells were collected and starved on non-nutrient agar for 2–3 h (early cells) or 5–6 h (late cells). Cells were then harvested, suspended in 10 mM KH_2PO_4/Na_2HPO_4, pH 6.5 (phosphate buffer, PB), and used in experiments. Confocal images were recorded using a Zeiss LSM800 confocal laser scanning microscope equipped with a Zeiss plan-apochromatic 63× numerical aperture 1.4 objective.

A sensitive assay for Ras activation at the cell boundary

RBD-Raf–GFP binds to the active form of Ras in the plasma membrane. Pixels with the plasma membrane also contain an unknown amount of cytosol with RBD-Raf–GFP. By co-expressing RBD-Raf–GFP and cytosolic RFP we were able to use the RFP signal to estimate the cytosolic volume, which allows us to calculate the amount of RBD-Raf-GFP that specifically binds to Ras-GTP at the membrane (Bosgraaf et al., 2008; Kortholt et al., 2013). For calculations, we used the following steps. First, the images of the movie are corrected, if needed, for bleaching by using the EMBL ImageJ plugin Bleach corrector; usually the RFP signal shows ∼10–30% bleaching during 5 min. Then the mean background fluorescence intensity in the red and green channels outside the cells was determined and subtracted from all pixels of the movie. Subsequently individual cells are analyzed. To correct for the difference in expression levels of the two markers within one cell, large areas of the cytoplasm were selected (excluding the nucleus and vacuoles), yielding the mean fluorescent intensity in the cytoplasm of the red channel $\langle R_c \rangle$ and green channel $\langle G_c \rangle$, respectively. This provided the correction factor $c=\langle G_c \rangle / \langle R_c \rangle$, and all pixels in the red channel were multiplied by c. Then for each pixel (i) of that cell we calculated the difference between the green and corrected red signal, and this was normalized by dividing by the average fluorescent intensity of GFP in the cytoplasm. Thus, the amount of RBD-Raf–GFP that specifically binds to Ras-GTP at the membrane in pixel (i) is given by $\Psi(i)=(G_i-cR_i)/\langle G_c \rangle$. Previous analysis with a phosphatidylinositol (3,4,5)-trisphosphate (PIP3) detector (Bosgraaf et al., 2008) and the current Ras-GTP detector (Kortholt et al., 2013) reveals that this method provides a ∼10-fold increase of sensitivity for the detection of local activated Ras.

The recordings of Ras activation in *iqgap2*-null+LatA cells was challenging, because Ras activation in patches appears to be very sensitive to laser light. In *iqgap2*-null cells treated for 10 min with 5 µM LatA, we observed some Ras-GTP patches in the first image taken (cell about 1.5 s scanning exposure) that rapidly disappear in the subsequent ten images (taken at a 1.63 s interval). Then another part of the same plate was observed, showing cells with a similar amount of Ras-GTP patches that also rapidly disappear in subsequent images. Kinetic analysis revealed that the loss RDP-Raf–GFP in patches starts at 7 s after the onset of laser exposure and exhibits first-order kinetics with a half time of only ∼15 s. We performed an experiment to investigate the effect of laser light on *iqgap2*-null+LatA cells. Images with 1 s exposure were recorded every 10 s; during the 9 s intervals cells were either exposed to constant laser scanning or not exposed. We observed that continued laser scanning exposure leads to the rapid loss of Ras-GTP patches, while the cells not exposed to laser scanning in the intervals retained Ras-GTP patches and also formed new Ras-GTP patches, even after 20 min. Further analysis revealed that basal Ras-GTP levels at the boundary in between Ras-GTP patches was not reduced during continued laser scanning exposure of *iqgap2*-null+LatA cells, suggesting that laser light rapidly inhibits Ras-GTP excitability in these cells.

Subsequently, we inspected all other cell lines and conditions for laser sensitivity, but did not find deleterious effects (including *iqgap2*-null cells without LatA) provided that cell recordings did not last longer than 5 min. Data for *iqgap2*-null+LatA cells were recorded with minimal exposure to laser light.

Data analysis

Images were analyzed with ImageJ. A line scan of three pixels wide was made at the boundary of the cell (see line scans of Fig. 3). The mean intensity $<\Psi>$ and the relative SD (heterogeneity ζ) were calculated for each line scan. Patches were identified according to the definition as a group of adjacent pixels with an intensity of $\Psi>0.2$, a width of at least 1 µm, and a duration of at least 8 s (van Haastert et al., 2017); for the static 3D image (Fig. 1) a minimal width and height of 1 µm was applied. Images were analyzed for rotational, reflection and left–right asymmetry as indicated below. Pseudopod extensions and cell displacement was determined from phase-contrast movies as described previously (Bosgraaf and Van Haastert, 2009b). Briefly, the start and end of the extension of a protrusion is indicated with an arrow. Protrusions that start at the right side relative to the end of the previous protrusion are defined 'right'. The left–right zig-zag bias of pseudopod extensions is defined as zig-zag bias [=(RL+LR)/(RR+LL)], where R is right and L is left.

Quantification of rotational and reflection symmetry

Definitions

An object is symmetric when the shape of the object does not change after rotation, reflection or translation (see Fig. S2). An object with rotational symmetry of the order n does not change its appearance when rotated around a central point at 360/n degrees. An object with reflection symmetry does not change its shape when reflected in a mirror. Many objects with rotational symmetry also have reflection symmetry (e.g. number 8), but not all (e.g. letter Z). An object with translational symmetry does not change its appearance when it is translated (relocated) in space or time. An object with gliding reflection symmetry is the combination of a translation and a reflection; an example is the imprint of footsteps of human gait, and – very relevant for the current study – the way how polarized cells move. Cells with patches of activated Ras at the cell boundary can have rotational or reflection symmetry. A cell with rotational symmetry always has reflection symmetry as well.

Quantifying rotational symmetry

The method has been used to describe radial structures such as the petals of flowers or chemical structures (Frey et al., 2007). In this paragraph, a mathematical description of symmetry is provided; Figs S3 and S4 show graphical representations of this analysis. Our objects have patches of activated Ras, such as Fig. 7A–C for an unpolarized cell. Each patch (i) has a magnitude P_i and an angle relative to the adjacent patch φ_i. The averages of all patches are $<P_i>=\alpha$ and $<\varphi_i>=\beta$. The order of rotational symmetry is n; therefore $\beta=360/n$.

The deviation from perfect rotational symmetry (=asymmetry) for patch (i) is given by:

$$d(P_i, \varphi_i) = \alpha^2 + P_i^2 - 2\alpha P_i \cos(\varphi_i - \beta),$$

and the deviation from perfect rotational symmetry for n patches is given by:

$$s = < d(P_i, \varphi_i) > .$$

The value of asymmetry s is between 0 and 1, with $s=0$ for perfect rotational symmetry.

Determination of the order of rotational symmetry

Cells exhibit multiple patches of activated Ras; some patches are large, others are smaller. The Ras patches are numbered sequentially with decreasing intensity. In Fig. 7B, ten patches are detectable for that specific cell. We determined asymmetry s for different symmetry orders starting from 3, always incorporating the strongest patches (thus, order n uses patches numbered 1 to n).

In the Results section, we defined Ras patches as areas of connecting pixels with a minimum width of 1 µm, intensity $\Psi>0.2$ and duration of 8 s. In the analysis of symmetry, we also consider areas of Ras patches that are of smaller size and/or lower intensity. The reason is related to the fundamental principle of symmetry analysis of imperfect structures: assume a 'perfect' flower with six petals that has strong six-fold symmetry because the petals are about equal in length and at 60 degrees angles. Now remove one petal and ask whether it has still six-fold symmetry (implying one petal has zero length), or five-fold symmetry (implying that many angles deviate from the optimal 72 degrees). Obviously both 5-fold and 6-fold symmetries of this imperfect 5-petal flower are much lower than the 6-fold symmetry of the original 6-petal flower. Calculations using the equations above show that the optimal rotational symmetry for this imperfect flower is 6-fold symmetry. The distribution of Ras patches is not very regular, with patches of unequal intensity and angles. To find the optimal symmetry order (n), we included increasing numbers of potential patches, and also small patches; then the statistical analysis provides the optimal symmetry order (see Figs S3 and S4).

The Akaike Information Criterion (AIC) was used to determine the best order of symmetry, with the general format:

$$AIC = 2k + m\ln(RSS/m),$$

where k is the number of parameters, m is the number of measurements and RSS/m is used as the likelihood of the fit. Since the measure of asymmetry s is an optimization procedure (0 for perfect symmetry, 1 for random), we take $RSS/m=s$. The number of parameters k is related to n, the order of symmetry; $k=2n-1$ because there are n intensities and $n-1$ angles (the sum of angles is 360 degrees). The number of measurements is the number of patches of the model (i.e. $m=n$). Thus, for rotational symmetry:

$$AIC = 2(2n - 1) + n\ln(s).$$

AIC values were determined for different orders of symmetry; the model with the lowest AIC value is the preferred model (AIC1). The probability relative to model 1 that the model 2 with the second lowest value (AIC2) is the preferred model is given by:

$$P = e^{(AIC1 - AIC2)/2}.$$

In this way, a probability is attributed to each model inspected for rotational symmetry, providing a probabilistic estimate of the optimal order n of rotational symmetry (Fig. 7D).

Quantifying reflection symmetry

The method for quantifying reflection symmetry is an adaptation of the method described above for rotational symmetry. It requires additional definitions for the symmetry axis and for odd versus even number of patches (see Fig. 7E). Here patches are also numbered in sequential order of declining intensity, and patches 1 to n are used to quantify the nth order of symmetry.

A cell with reflection symmetry of activated Ras patches must have an axis of symmetry. We make the assumption that the axis of reflection symmetry is defined by the midpoint of P1, the strongest patch. This assumption is based on the observation that pseudopod extension is induced at the position of the strongest Ras patch (van Haastert et al., 2017). Thus, for reflection symmetry P1 is always at the reflection axis. As with rotational symmetry, each patch (i) has a magnitude P_i; the angle of the patches is here not the angle φ_i relative to the next patch, but the angle θ_i relative to the axis of symmetry. For an odd number of patches, the other patches are attributed as pairs; a pair has one patch at each side of the symmetry axis (in Fig. 7F: for $n=5$, the pairs are P3+P4 and P2+P5). For an even number of patches, two patches are at the symmetry axis, P1 and the patch closest to the opposite side of the cell; the other patches are again attributed as pairs (in Fig. 7F for $n=4$, P5 is not used, P1 and P2 are positioned to the symmetry axis and P3 and P4 form a pair).

The deviation from perfect reflection symmetry for each patch in a pair is given by:

$$d(P_i, \theta_i) = \alpha^2 + P_i^2 - 2\alpha P_i \cos(\theta_i - \beta).$$

Now, α and β are the averages of length and angle for the two patches of that pair.

For an even number of patches, the patch P_R opposite to P1 has specific properties with $\alpha=P_R$ and $\beta=0$. The deviation of P_R from perfect reflection symmetry is given by:

$$d(P_R, \theta_R) = 2P_R^2(1-\cos\theta_R).$$

Again the asymmetry of all patches is given by the average of the deviation of all patches:

$$s = < d(P_i, \theta_i), d(P_R, \theta_R) >$$

Determination of the order of reflection symmetry

The optimal order for reflection symmetry is determined as for rotation symmetry using AIC and probability distribution, $AIC=2(2n-1)+n\ln(s)$ and $P=e^{(AIC1-AIC2)/2}$, respectively.

Discrimination between rotational and reflection symmetry.

The general equation for AIC is used to select the optimal model, $AIC=2k+m\ln(RSS/m)$. Here, model discrimination is not about the order of symmetry, but about discrimination between rotation versus reflection, and therefore the number of parameters k has a different meaning. The parameters that characterize rotation symmetry are α and β, thus $k=2$ for rotation, independently of the number of patches. However, for reflection symmetry α and β have different values for each pair of patches, and therefore reflection symmetry has two parameters for each pair of patches. For an odd number of patches, there are $(n-1)/2$ pairs, thus $k=n-1$ parameters; for an even number patches, there are $(n-2)/2$ pairs plus θ_R, thus also $k=n-1$ parameters. The number of independent measurements (m) is the number of patches for rotation ($m=n$); for reflection P1 is fixed at the symmetry axis, so, for rotation, $m=n-1$. Therefore, model discrimination between rotation and reflection is tested with:

$$AIC_t = 2 + n\ln(s_t) \text{ versus } AIC_f = 2(n-1) + (n-1)\ln(s_f),$$

where the subscript t and f refer to rotation and reflection, respectively. The AIC with the lowest value is the preferred model. The probability of the best versus the second best model is given by:

$$P = e^{(AIC1-AIC2)/2}.$$

Please note that reflection symmetry is characterized by more parameters than rotation symmetry. Accordingly, AIC penalizes reflection stronger than rotation. Therefore, an object that has both rotational and reflection symmetry (the shape of number 8, or Ras-GTP patches in unpolarized cells) is identified with rotational symmetry.

Quantifying left–right asymmetry

In reflection symmetry, P1 is part of the symmetry axis with patches at the left and right side of this symmetry axis (Fig. 7F). We determined how symmetric the patches are in respect to their intensities. Thus, in the Fig. 7F, we estimate how different are P3 and P4 and how different are P2 and P5. The left–right asymmetry for a pair of patches was calculated as the difference between the intensity of the left and right patch relative to the sum of intensities of left and right:

$$LR\_asymmetry = \frac{|P_{left} - P_{right}|}{P_{left} + P_{right}}$$

LR_asymmetry is between 0 and 1, with 0 for perfect symmetry when $P_{left}=P_{right}$, and 1 for perfect asymmetry when P_{left} or $P_{right}=0$. For Fig. 7F, the asymmetry of patches P3 and P4 is 0.11, and of P2 and P5 is 0.40. The LR_asymmetry around the strongest patch is thus 0.11, whereas the total LR_asymmetry of the cell is the average of the asymmetries of all pairs of patches (i.e. 0.26). We report on the LR_asymmetry around the strongest patch.

Statistics and re-use of data

All data shown are the mean±s.d. or s.e.m. with the number of replicates (n) as indicated in the figure legends or text. Statistical significance was tested with a Student's t-test. The Akaike Information Criterion (AIC) was used to discriminate between different models as indicated above. The experiments on Ras activation in wild-type cells were performed previously (van Haastert et al., 2017) and original data, sometimes supplemented with new experiments to enlarge the dataset, were reused for the new analysis on symmetry (Figs 2A,G and 3A,B, and wild-type in 5C).

Acknowledgements

We thank Richard Firtel (Section of Cell and Developmental Biology, University of California, San Diego, USA) for the *iqgap* and *ctx* null cells, Jan Faix (Institute for Biophysical Chemistry, Hannover Medical School, Germany) for *mdia* and *airpin*-null cells and Robert Insall (Cancer Research UK Beatson Institute, Glasgow, UK) for *scar*-null and Scar-S55D cells.

Competing interests

The authors declare no competing or financial interests.

Author contributions

Conceptualization: P.J.M.v.H., A.K.; Methodology: P.J.M.v.H., A.K., I.K.-G.; Validation: P.J.M.v.H.; Formal analysis: P.J.M.v.H.; Investigation: P.J.M.v.H., I.K.-G.; Writing - original draft: P.J.M.v.H., A.K.; Writing - review & editing: P.J.M.v.H., A.K.; Visualization: P.J.M.v.H.; Project administration: P.J.M.v.H.; Funding acquisition: P.J.M.v.H., A.K.

Funding

This work has been supported by a Nederlandse Organisatie voor Wetenschappelijk Onderzoek (Netherlands Organization for Scientific Research) NWO-VIDI grant (723.012.108) to A.K.

Supplementary information

Supplementary information available online at
http://jcs.biologists.org/lookup/doi/10.1242/jcs.208892.supplemental

References

Blum, M., Schweickert, A., Vick, P., Wright, C. V. and Danilchik, M. V. (2014). Symmetry breakage in the vertebrate embryo: when does it happen and how does it work? *Dev. Biol.* **393**, 109-123.

Bosgraaf, L. and van Haastert, P. J. M. (2006). The regulation of myosin II in Dictyostelium. *Eur. J. Cell Biol.* **85**, 969-979.

Bosgraaf, L. and Van Haastert, P. J. M. (2009a). Navigation of chemotactic cells by parallel signaling to pseudopod persistence and orientation. *PloS ONE* **4**, e6842.

Bosgraaf, L. and Van Haastert, P. J. M. (2009b). The ordered extension of pseudopodia by amoeboid cells in the absence of external cues. *PloS ONE* **4**, e5253.

Bosgraaf, L., Keizer-Gunnink, I. and Van Haastert, P. J. M. (2008). PI3-kinase signaling contributes to orientation in shallow gradients and enhances speed in steep chemoattractant gradients. *J. Cell Sci.* **121**, 3589-3597.

Charest, P. G. and Firtel, R. A. (2006). Feedback signaling controls leading-edge formation during chemotaxis. *Curr. Opin. Genet. Dev.* **16**, 339-347.

Charest, P. G. and Firtel, R. A. (2007). Big roles for small GTPases in the control of directed cell movement. *Biochem. J* **401**, 377-390.

Charest, P. G., Shen, Z., Lakoduk, A., Sasaki, A. T., Briggs, S. P. and Firtel, R. A. (2010). A Ras signaling complex controls the RasC-TORC2 pathway and directed cell migration. *Dev. Cell* **18**, 737-74.

Dang, I., Gorelik, R., Sousa-Blin, C., Derivery, E., Guérin, C., Linkner, J., Nemethova, M., Dumortier, J. G., Giger, F. A., Chipysheva, T. A. et al. (2013). Inhibitory signalling to the Arp2/3 complex steers cell migration. *Nature* **503**, 281-284.

Davidson, A. J. and Insall, R. H. (2013). SCAR/WAVE: a complex issue. *Commun. Integr. Biol.* **6**, e27033.

Davidson, A. J., Amato, C., Thomason, P. A. and Insall, R. H. (2017). WASP family proteins and formins compete in pseudopod- and bleb-based migration. *J. Cell Biol.* **217**, 701-714.

Devreotes, P. and Horwitz, A. R. (2015). Signaling networks that regulate cell migration. *Cold Spring Harbor Perspect. Biol.* **7**, a005959.

Faix, J. and Weber, I. (2013). A dual role model for active Rac1 in cell migration. *Small GTPases* **4**, 110-115.

Filić, V., Marinovic, M., Faix, J. and Weber, I. (2012). A dual role for Rac1 GTPases in the regulation of cell motility. *J. Cell Sci.* **125**, 387-398.

Filić, V., Marinović, M., Faix, J. and Weber, I. (2014). The IQGAP-related protein DGAP1 mediates signaling to the actin cytoskeleton as an effector and a sequestrator of Rac1 GTPases. *Cell. Mol. Life Sci.* **71**, 2775-2785.

Frey, F. M., Robertson, A. and Bukoski, M. (2007). A method for quantifying rotational symmetry. *New Phytol.* **175**, 785-791.
Girard, K. D., Chaney, C., Delannoy, M., Kuo, S. C. and Robinson, D. N. (2004). Dynacortin contributes to cortical viscoelasticity and helps define the shape changes of cytokinesis. *EMBO J.* **23**, 1536-1546.
Goryachev, A. B. and Leda, M. (2017). Many roads to symmetry breaking: molecular mechanisms and theoretical models of yeast cell polarity. *Mol. Biol. Cell* **28**, 370-380.
Gross, D. J. (1996). The role of symmetry in fundamental physics. *Proc. Natl. Acad. Sci. USA* **93**, 14256-14259.
Huang, C.-H., Tang, M., Shi, C., Iglesias, P. A. and Devreotes, P. N. (2013). An excitable signal integrator couples to an idling cytoskeletal oscillator to drive cell migration. *Nat. Cell Biol.* **15**, 1307-1316.
Inoue, T. and Meyer, T. (2008). Synthetic activation of endogenous PI3K and Rac identifies an AND-gate switch for cell polarization and migration. *PloS ONE* 3, e3068.
Insall, R. (2013). The interaction between pseudopods and extracellular signalling during chemotaxis and directed migration. *Curr. Opin. Cell Biol.* **25**, 526-531.
Jeon, T. J., Lee, D.-J., Merlot, S., Weeks, G. and Firtel, R. A. (2007). Rap1 controls cell adhesion and cell motility through the regulation of myosin II. *J. Cell Biol.* **176**, 1021-1033.
Jin, T. (2013). Gradient sensing during chemotaxis. *Curr. Opin. Cell Biol.* **25**, 532-537.
Johnson, H. E., King, S. J., Asokan, S. B., Rotty, J. D., Bear, J. E. and Haugh, J. M. (2015). F-actin bundles direct the initiation and orientation of lamellipodia through adhesion-based signaling. *J. Cell Biol.* **208**, 443-455.
Kee, Y.-S., Ren, Y., Dorfman, D., Iijima, M., Firtel, R., Iglesias, P. A. and Robinson, D. N. (2012). A mechanosensory system governs myosin II accumulation in dividing cells. *Mol. Biol. Cell* **23**, 1510-1523.
Kimura, K., Ito, M., Amano, M., Chihara, K., Fukata, Y., Nakafuku, M., Yamamori, B., Feng, J., Nakano, T., Okawa, K. et al. (1996). Regulation of myosin phosphatase by Rho and Rho-associated kinase (Rho-kinase). *Science* **273**, 245-248.
Kortholt, A. and van Haastert, P. J. M. (2008). Highlighting the role of Ras and Rap during Dictyostelium chemotaxis. *Cell. Signal.* **20**, 1415-1422.
Kortholt, A., Keizer-Gunnink, I., Kataria, R. and Van Haastert, P. J. M. (2013). Ras activation and symmetry breaking during Dictyostelium chemotaxis. *J. Cell Sci.* **126**, 4502-4513.
Köster, D. V. and Mayor, S. (2016). Cortical actin and the plasma membrane: inextricably intertwined. *Curr. Opin. Cell Biol.* **38**, 81-89.
Krause, M. and Gautreau, A. (2014). Steering cell migration: lamellipodium dynamics and the regulation of directional persistence. *Nat. Rev. Mol. Cell Biol.* **15**, 577-590.
Kureishi, Y., Kobayashi, S., Amano, M., Kimura, K., Kanaide, H., Nakano, T., Kaibuchi, K. and Ito, M. (1997). Rho-associated kinase directly induces smooth muscle contraction through myosin light chain phosphorylation. *J. Biol. Chem.* **272**, 12257-12260.
Lee, S., Shen, Z., Robinson, D. N., Briggs, S. and Firtel, R. A. (2010). Involvement of the cytoskeleton in controlling leading-edge function during chemotaxis. *Mol. Biol. Cell* **21**, 1810-1824.
Li, L., Nørrelykke, S. F. and Cox, E. C. (2008). Persistent cell motion in the absence of external signals: a search strategy for eukaryotic cells. *PloS ONE* **3**, e2093.
Livio, M. (2012). Physics: why symmetry matters. *Nature* **490**, 472-473.
Loh, K. M., van Amerongen, R. and Nusse, R. (2016). Generating cellular diversity and spatial form: Wnt signaling and the evolution of multicellular animals. *Dev. Cell* **38**, 643-655.
McDowell, G. S., Lemire, J. M., Paré, J.-F., Cammarata, G., Lowery, L. A. and Levin, M. (2016). Conserved roles for cytoskeletal components in determining laterality. *Integr. Biol. (Camb).* **8**, 267-286.
Meili, R., Alonso-Latorre, B., del Alamo, J. C., Firtel, R. A. and Lasheras, J. C. (2010). Myosin II is essential for the spatiotemporal organization of traction forces during cell motility. *Mol. Biol. Cell* **21**, 405-417.
Miao, Y., Bhattacharya, S., Edwards, M., Cai, H., Inoue, T., Iglesias, P. A. and Devreotes, P. N. (2017). Altering the threshold of an excitable signal transduction network changes cell migratory modes. *Nat. Cell Biol.* **19**, 329-340.
Mondal, S., Burgute, B., Rieger, D., Müller, R., Rivero, F., Faix, J., Schleicher, M. and Noegel, A. A. (2010). Regulation of the actin cytoskeleton by an interaction of IQGAP related protein GAPA with filamin and cortexillin I. *PloS ONE* **5**, e15440.
Ngo, K. X., Umeki, N., Kijima, S. T., Kodera, N., Ueno, H., Furutani-Umezu, N., Nakajima, J., Noguchi, T. Q. P., Nagasaki, A., Tokuraku, K. et al. (2016). Allosteric regulation by cooperative conformational changes of actin filaments drives mutually exclusive binding with cofilin and myosin. *Sci. Rep.* **6**, 35449.
Nichols, J. M., Veltman, D. and Kay, R. R. (2015). Chemotaxis of a model organism: progress with Dictyostelium. *Curr. Opin. Cell Biol.* **36**, 7-12.
Pillitteri, L. J., Guo, X. and Dong, J. (2016). Asymmetric cell division in plants: mechanisms of symmetry breaking and cell fate determination. *Cell. Mol. Life Sci.* **73**, 4213-4229.
Plak, K., Keizer-Gunnink, I., van Haastert, P. J. M. and Kortholt, A. (2014). Rap1-dependent pathways coordinate cytokinesis in Dictyostelium. *Mol. Biol. Cell* **25**, 4195-4204.
Ramalingam, N., Franke, C., Jaschinski, E., Winterhoff, M., Lu, Y., Brühmann, S., Junemann, A., Meier, H., Noegel, A. A., Weber, I. et al. (2015). A resilient formin-derived cortical actin meshwork in the rear drives actomyosin-based motility in 2D confinement. *Nat. Commun.* **6**, 8496.
Ren, Y., Effler, J. C., Norstrom, M., Luo, T., Firtel, R. A., Iglesias, P. A., Rock, R. S. and Robinson, D. N. (2009). Mechanosensing through cooperative interactions between myosin II and the actin crosslinker cortexillin I. *Curr. Biol.* **19**, 1421-1428.
Rensing, S. A. (2016). (Why) does evolution favour embryogenesis? *Trends Plant Sci.* **21**, 562-573.
Ruppel, K. M., Uyeda, T. Q. and Spudich, J. A. (1994). Role of highly conserved lysine 130 of myosin motor domain. In vivo and in vitro characterization of site specifically mutated myosin. *J. Biol. Chem.* **269**, 18773-18780.
Sackmann, E. (2015). How actin/myosin crosstalks guide the adhesion, locomotion and polarization of cells. *Biochim. Biophys. Acta* **1853**, 3132-3142.
Sasaki, A. T., Janetopoulos, C., Lee, S., Charest, P. G., Takeda, K., Sundheimer, L. W., Meili, R., Devreotes, P. N. and Firtel, R. A. (2007). G protein-independent Ras/PI3K/F-actin circuit regulates basic cell motility. *J. Cell Biol.* **178**, 185-191.
Schwamborn, J. C. and Püschel, A. W. (2004). The sequential activity of the GTPases Rap1B and Cdc42 determines neuronal polarity. *Nat. Neurosci.* **7**, 923-929.
Shi, C., Huang, C. H., Devreotes, P. N. and Iglesias, P. A. (2013). Interaction of motility, directional sensing, and polarity modules recreates the behaviors of chemotaxing cells. *PLoS Comput. Biol.* **9**, e1003122.
Tang, M., Wang, M., Shi, C., Iglesias, P. A., Devreotes, P. N. and Huang, C. H. (2014). Evolutionarily conserved coupling of adaptive and excitable networks mediates eukaryotic chemotaxis. *Nat. Commun.* **5**, 5175.
Taniguchi, D., Ishihara, S., Oonuki, T., Honda-Kitahara, M., Kaneko, K. and Sawai, S. (2013). Phase geometries of two-dimensional excitable waves govern self-organized morphodynamics of amoeboid cells. *Proc. Natl Acad. Sci. USA* **110**, 5016-5021.
Ura, S., Pollitt, A. Y., Veltman, D. M., Morrice, N. A., Machesky, L. M. and Insall, R. H. (2012). Pseudopod growth and evolution during cell movement is controlled through SCAR/WAVE dephosphorylation. *Curr. Biol.* **22**, 553-561.
Van Haastert, P. J. M. and Bosgraaf, L. (2009). Food searching strategy of amoeboid cells by starvation induced run length extension. *PloS ONE* **4**, e6814.
van Haastert, P. J. M., Keizer-Gunnink, I. and Kortholt, A. (2017). Coupled excitable Ras and F-actin activation mediates spontaneous pseudopod formation and directed cell movement. *Mol. Biol. Cell* 28, 922-934.
Veltman, D. M., Williams, T. D., Bloomfield, G., Chen, B.-C., Betzig, E., Insall, R. H. and Kay, R. R. (2016). A plasma membrane template for macropinocytic cups. *Elife* **5**, e20085.
Wennekamp, S., Mesecke, S., Nédélec, F. and Hiiragi, T. (2013). A self-organization framework for symmetry breaking in the mammalian embryo. *Nat. Rev. Mol. Cell Biol.* **14**, 452-459.
Yang, H. W., Collins, S. R. and Meyer, T. (2016). Locally excitable Cdc42 signals steer cells during chemotaxis. *Nat. Cell Biol.* **18**, 191-201.